


Revisiting the Role of Metallic Antennas to Control Light Emission by Lead Salt Nanocrystal Assemblies

Hongyue Wang,¹ Abdelhanin Aassime,¹ Xavier Le Roux,¹ Nick J. Schilder,² Jean-Jacques Greffet,^{2,*} and Aloyse Degiron^{1,†}

¹*Centre de Nanosciences et de Nanotechnologies, CNRS, Univ. Paris-Sud, Université Paris-Saclay, C2N–Orsay, 91405 Orsay cedex, France*

²*Laboratoire Charles Fabry, Institut d'Optique Graduate School, CNRS, Université Paris-Saclay, 91127 Palaiseau Cedex, France*

 (Received 22 May 2018; revised manuscript received 27 July 2018; published 20 September 2018)

Thin films of lead salt nanocrystals (NCs) offer attractive opportunities as active media for near-infrared optoelectronics but suffer from limiting trade-offs between optical and electrical properties. While NCs separated by nanometer-long ligands are good light emitters, NCs capped with shorter molecules provide a high carrier mobility but degrade the photo- and electroluminescence and broaden the narrow emission spectrum. Here we show that this severe quenching and spectral broadening can be averted with an unconventional use of metallic antennas. The resulting NC-antenna hybridization not only provides a strong boost in luminescence, but also makes it possible to remodel the emission spectrum in radical ways, even at wavelengths where the NC assembly does not emit light. These results cannot be explained with the standard theory of single-emitter luminescence assisted by optical antennas. We propose an alternative model based on a statistical description of light emission by an ensemble of emitters and discuss important consequences of our findings for nano-optics and solution-processed optoelectronics.

DOI: [10.1103/PhysRevApplied.10.034042](https://doi.org/10.1103/PhysRevApplied.10.034042)

I. INTRODUCTION

The trade-offs between optical properties and electrical transport can be appreciated in Fig. 1 where we show the characteristics of a film of PbS nanocrystals before and after exchange of the native 2-nm-long trioctylphosphine oxide (TOPO) ligands by dangling S^{2-} ions. The evolution of the photoluminescence [PL, Fig. 1(a)], absorption [Fig. 1(b)], and electrical conductivity [Fig. 1(c)] is consistent with the literature [1–4]. Before ligand exchange, the PL and absorption spectra feature an excitonic peak and the electrical transport is poor because the insulating ligands force the carriers to hop from one NC to another [5]. After treating the NC film with a solution of Na_2S in ethanol to replace the TOPO ligands by sulfur ions, the conductivity improves but the PL is almost entirely suppressed, with a reduction of more than two orders of magnitude of the signal. This severe quenching is accompanied by a sizeable broadening and redshift of both PL and absorption peaks. This behavior suggests that the PbS nanocrystals are now sufficiently close to each other that their mutual interactions are dominated by electronic coupling, leading to nonradiative charge transfer to neighboring NCs and a

loss of quantum confinement that shifts the spectral properties toward those of bulk PbS [2,4,6]. It is also likely that defects caused by oxidation reinforce these trends because our samples are made under ambient atmosphere.

While the luminescence of compact NC assemblies can be partially recovered by lowering the temperature to a few tens of kelvins, it has little potential for practical applications and is essentially used for understanding the fundamental mechanisms at play in NC-based solar cells [6–8]. In this article, we show how to achieve the same feat at room temperature using arrays of Au antennas that also restore sharp and tunable properties despite the poor quantum confinement within the NC assembly.

To this aim, let us consider the light-emitting diode (LED) architecture represented in Fig. 1(d). The Au inclusions are defined by electron-beam lithography and two monolayers of ligand-exchanged PbS NCs form a conformal coating above them. This PbS/Au heterostructure is electrically addressed on the bottom side by an Al cathode and a TiO_2 electron transfer layer and on the top side by a MoO_x hole transfer layer and a transparent indium tin oxide (ITO) anode. We already introduced variants of the same architecture (albeit with NCs capped with native ligands) to demonstrate electroluminescent metasurfaces with complex gradients in their optoelectronic properties [9,10]. Here, we use the structure of Fig. 1(a) for a different purpose, namely to alleviate the trade-offs

*jean-jacques.greffet@institutoptique.fr

†aloyse.degiron@u-psud.fr

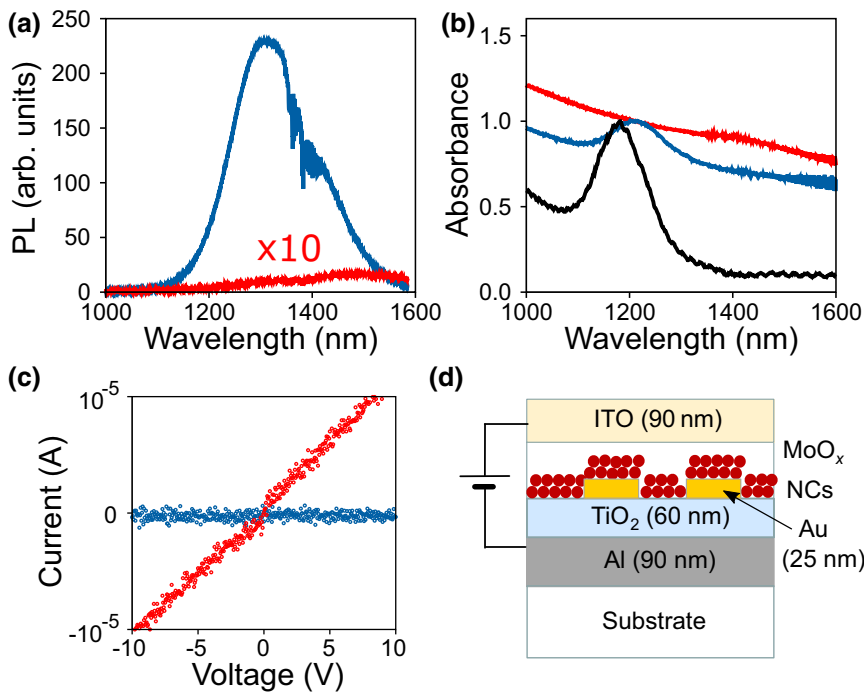


FIG. 1. (a) Photoluminescence intensity of a NC film before and after ligand exchange (blue and red curves, respectively). The noisy shoulder between 1345 and 1480 nm is an experimental artifact due to the absorption lines of the atmosphere. (b) Absorbance of a NC film before and after ligand exchange [same color code as panel (a)]. The black curve represents the absorbance of the PbS nanocrystals in solution. The different traces are offset for clarity. (c) Current vs voltage between two Au pads connected with PbS NCs. The distance between the two Au pads is 20 μm and the PbS NCs are drop-cast in the slit between the pads. Blue curve: result before ligand exchange; red curve: result after ligand exchange. (d) Schematic view of the LEDs considered in the remainder of the study.

between luminescence, loss of quantum confinement, and electrical conductivity in ensembles of PbS NCs, and to discuss an important paradigm shift for optical antennas as a consequence of our findings.

II. RESULTS AND DISCUSSION

We first consider a device operating with nonresonant Au nanodiscs. Figure 2(a) shows the reflectivity spectrum obtained by illuminating the structure through the transparent anode. The reflectivity is high and rather uniform because the nonresonant nanodiscs only weakly perturb the incoming light as it is reflected by the bottom Al electrode. Yet, the PL spectrum, represented in Fig. 2(b), shows that more light is emitted compared to the PL measured on a reference device without Au nanoparticles. Moreover, it has a complex shape with three maxima located at 1450, 1280, and 1150 nm. The same three peaks are also observed in the electroluminescence (EL) spectrum [Fig. 2(c)] and the light-voltage curves of Fig. 2(g) show that the Au nanodiscs reduce the turn-on voltage from 8 V for the reference sample to 2 V.

We have then repeated the experiments using resonant Au nanoparticles [Figs. 2(d)–(f)]. The new array, which combines rings and discs, has also been designed to have a relatively flat reflectivity spectrum but with a much lower baseline thanks to the excitation of surface plasmons. The PL and EL spectra feature the same three peaks as before, albeit with a modified weight and a much larger amplitude. The increased luminescence is particularly spectacular for the EL, as can be appreciated in a quantitative way on the light-voltage curves of Fig. 2(g): the LED with resonant

Au particles is 10 to 100 times brighter than the LED operating with nonresonant Au discs and its turn-on voltage is only 1 V. In other words, we have been able to enhance the conductivity of the lead salt NC assembly (with the ligand exchange procedure) together with its luminescence (with the Au nanoparticles), thus overcoming the inherent trade-off between these parameters.

The results of Fig. 2 indicate that the Au particles play the role of optical antennas that boost and modify the PL and EL of the devices. It may be tempting to attribute these changes to the Purcell effect—the mechanism typically at play in such cases [11–13]. However, two key observations invalidate this hypothesis. First, the Purcell effect manifests itself as a change in the radiation decay rate but it does not affect the emission wavelength of the emitter [13]. In contrast, the measurements of Fig. 2 reveal the presence of new spectral features that are indistinctly obtained with resonant and nonresonant Au particles and that are not present in the spectra taken without the Au antenna. Second, it is well established that metallic antennas destroy the luminescence of emitters placed too close to them due to nonradiative losses [11–13]. This is another result that cannot be reconciled with our experiments since in our case, the NCs are directly coated onto the Au inclusions.

To explain the observations, it is important to make a distinction between the spontaneous emission of individual emitters and the spontaneous emission of an ensemble of highly coupled emitters such as our PbS NC assemblies. When excited by light or electricity, individual emitters usually relax to form one (or a few) exciton(s) between a hole and an electron separated by an energy gap. Because excitons can either decay through the emission of a photon

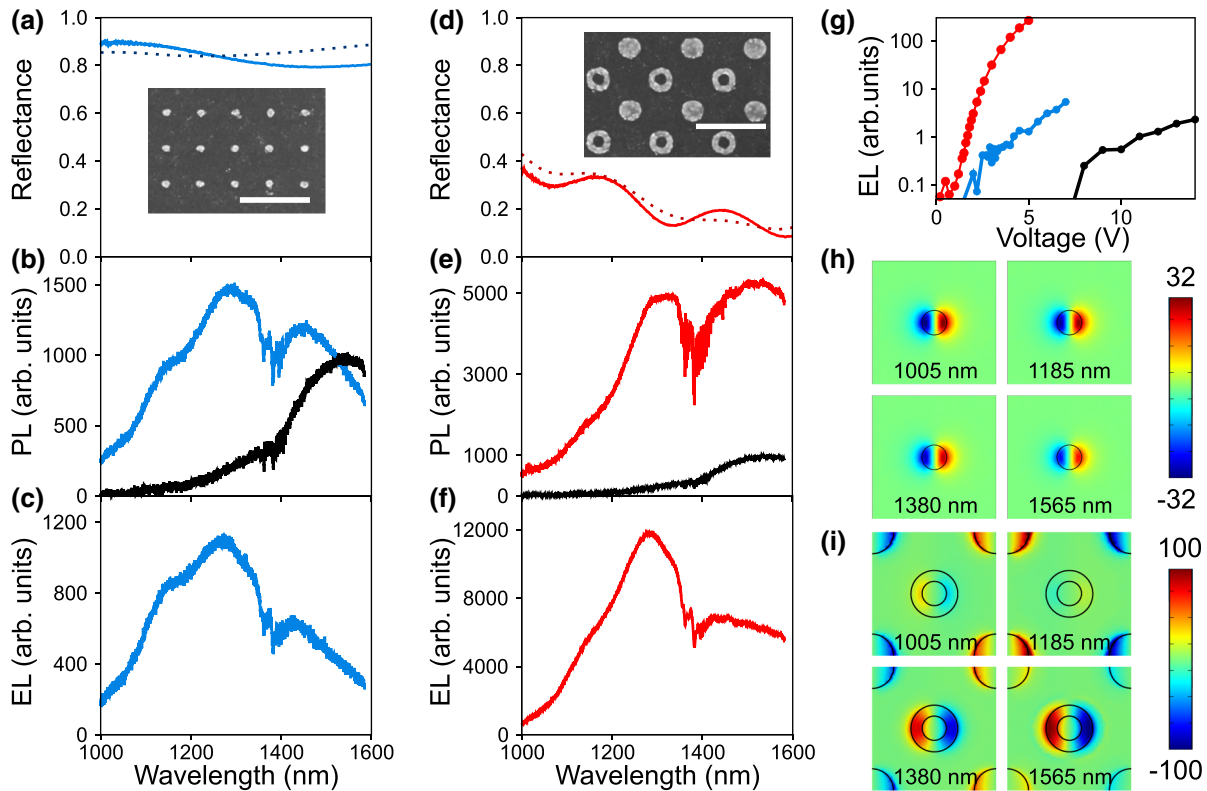


FIG. 2. (a) Reflectance of a LED operating with nonresonant Au nanodiscs. The continuous trace is the experimental spectrum and the dotted line is the result of finite-element simulations. Inset: SEM view of the nanoparticle array. Scale bar: 500 nm. (b),(c) PL and EL spectra of the structure with Au nanodiscs. The black trace on the PL plot is the spectrum of a reference LED without Au nanodiscs. (d)–(f) Same as panels (a)–(c), except for a LED operating with resonant Au discs and rings. (g) Light-voltage curves of the nonresonant and resonant structures considered in panels (a)–(f) (blue and red traces, respectively). Black curve: reference sample without Au nanostructure. (h) Finite-element simulations of the nonresonant structure with Au nanodiscs. Each plot represents the vertical component of the electric field in a unit cell at a different wavelength (1005, 1185, 1380, and 1565 nm). The structure is illuminated under normal incidence and the field is evaluated in a plane located 7.5 nm above the Au disc (outlined in black). (i) Same as panel (h) for the resonant structure with Au discs and rings. The field amplitude (in V m^{-1}) is roughly 3 times larger than for the nonresonant Au nanodiscs.

or via a nonradiative channel, optical antennas provide a powerful means to influence the competition between the two types of relaxation mechanisms. This is the Purcell effect discussed in the previous paragraph.

In contrast, emitters in close-packed NC assemblies are strongly influenced by their neighbors and it is well documented that their electronic structure can form energy bands as a result, even though their granularity, surface defects, disorder and polydispersity make them quite different from ideal homogeneous semiconducting materials [5]. A corollary is that electron-electron interaction, which is a much faster process than radiative recombination, leads to thermalization of the electrons (that is, they reach a thermodynamic equilibrium) in the conduction band. Similarly, holes thermalize and reach a thermodynamic equilibrium in the valence band. In both bands, the states are occupied according to a Fermi-Dirac distribution characterized by a quasi-Fermi-level, which depends on the

pumping intensity. This is a key difference from the single emitter where electrons and holes occupy the band edge states. Based on these arguments drawn from statistical physics, Würfel formally showed in 1982 that the PL and EL of homogeneous semiconductors is governed by the Kirchhoff law [14]—that is, the law that states that the emission intensity is proportional to the absorption cross section α of the material. Note that the Kirchhoff law also applies to thermal radiation as it corresponds to the special case of light emission due to electron-hole recombination in the absence of optical or electrical pumping.

Based on these considerations, one can expect that the same statistical treatment is also valid for NC assemblies. This analogy is already known and has been used, for example, to analyze the optoelectronic properties of an ensemble of Ag_2S NCs [15]. However, there exists an important difference between homogeneous conductors and NC assemblies on one hand, and our devices on

the other hand: the statistical treatment outlined above is only valid for homogeneous media and cannot be directly applied to our structures due to the presence of the Au antennas that induce strong nanoscale inhomogeneities.

To quantitatively account for the role of the antennas, we apply a model recently introduced for the electroluminescence of semiconductors mediated by resonant systems [16]. This model is a local form of the Kirchhoff law in which the key physical quantities (the carrier temperature T , the absorption cross section α , and the quasi-Fermi-levels for the valence and conduction bands) are defined locally in order to treat the case of inhomogeneous media. From this perspective, emission and absorption are described using Fermi-Dirac distributions, just as in the classical treatment by Würfel, except that they are locally modulated by the antennas. Hence, light appears to be due to emission by a bath of excited carriers mediated by the antennas. The intensity takes the form [16]:

$$I_e \propto \int_{\Omega} dx dy dz \alpha \frac{\omega^2}{4\pi^2 c^2} \frac{\hbar\omega}{\exp[(\hbar\omega - eV)/k_B T] - 1} \approx \left[\int_{\Omega} dx dy dz \alpha \exp(eV/k_B T) \right] I_W(\omega, T), \quad (1)$$

where α is the absorption cross-section density of the emitting layer at frequency ω and coordinates (x, y, z) , eV is the difference between the quasi-Fermi-levels at coordinates (x, y, z) , with e the electron charge and V the potential drop at the NC level (V is not the same for the NCs on the antennas and those outside the antennas but it is in all cases smaller than the applied bias voltage due to the resistances in the system), k_B is the Boltzmann constant, \hbar is the reduced Planck constant, and $I_W(\omega, T)$ is the Wien approximation of the blackbody radiance:

$$I_W(\omega, T) = \frac{\omega^2}{4\pi^2 c^2} \frac{\hbar\omega}{\exp(\hbar\omega/k_B T)} \quad (2)$$

The same formula is valid for PL provided that one replaces eV with the quasi-Fermi-level difference $\Delta\mu$ that depends on the optical pumping intensity. The main point of this model is that tailoring the emission properties at frequency ω is equivalent to act upon the absorption cross-section density α (at the same frequency). It is formally identical to the standard theory derived by Würfel for the EL and PL of bulk semiconductors where electrons and holes are held separately in local thermodynamic equilibrium [14]—but generalized to the case where α and eV exhibit spatial variations due to the presence of the Au antennas. In this stationary regime, the role of the Au antennas is to tailor α (i.e., the absorption by an ensemble of NCs in local thermodynamic equilibrium) with their local fields. This is a very different situation from the case

of the time-dependent decay of a single NC in the presence of an antenna with a competition between radiative and nonradiative decay rates [11–13].

It should be noted that despite the presence of $I_W(\omega, T)$ in Eq. (1), this model does not describe thermal radiation. Rather, $I_W(\omega, T)$ is directly related to the fact that the electrons and holes are independently in local thermodynamic equilibrium. As is the case for the standard Kirchhoff law, thermal radiation corresponds to the special case $eV=0$. When an external voltage bias (or an optical pump in the case of the PL experiments) is applied, light emission becomes significant regardless of the carrier temperature because of the factor $\exp(eV/k_B T)$. Since eV is typically in the order of the volt and $k_B T$ is 25 meV, emission may be significant even though α is much smaller than 1.

In summary, we interpret our experiments by the fact that the electron-electron interaction time is much faster than electron relaxation, and that all the electrons thermalize and are in local thermodynamic equilibrium as a result. Light is thus due to the electron-hole recombination between two crystal-like bands and not to the electron-hole recombination between the edge states in a particular NC. Emission is thus broadened. The coupling between the electromagnetic field and the bath of thermalized electrons and holes can be tailored by the design of an antenna. This antenna is a polarization and frequency-selective energy tap.

III. VALIDATION OF THE MODEL

The local fields that influence $\alpha(\omega, x, y, z)$ are represented in Figs. 2(h) and 2(i) for the two structures under consideration. These plots are obtained with a finite-element model that successfully reproduces the reflectance spectra of the structures [dotted lines on Figs. 2(a) and 2(d)]. The simulations show very good correlations with the properties of Figs. 2(a)–2(f). Specifically, the field distribution associated with the nonresonant structure is essentially constant across the whole spectral range and its amplitude is three times weaker than for the sample operating with discs and rings, in good agreement with the fact that the PL and EL spectra are broadband but much weaker than that for the resonant sample. The field distribution of the resonant structure exhibits more complex variations, with the high local fields being gradually displaced from the discs to the rings as the wavelength increases. Still, the fraction of the unit cell occupied by high local fields remains almost the same from one wavelength to the other, which is again consistent with the broadband PL and EL emissions measured for this sample.

Although these correlations are consistent with the local Kirchhoff law, there is a more compelling argument in favor of this scenario. According to Eq. (1), $\alpha(\omega, x, y, z)$ is not the only factor that influences the PL and EL spectra. They are also modulated by the Wien radiance $I_W(\omega, T)$

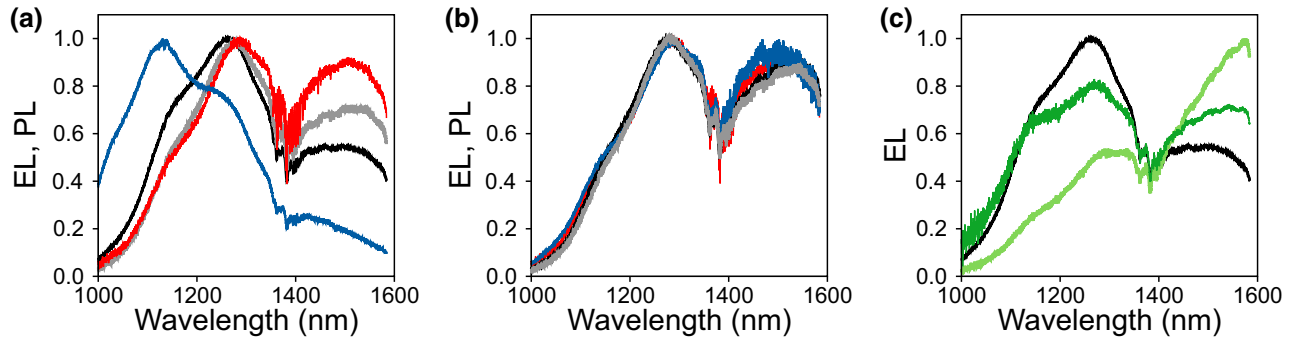


FIG. 3. (a) Red curve: PL spectrum of a sample with resonant discs and rings [same parameters as in Fig. 2(d)–(f)]. Gray and black curves: EL spectra of the sample biased at 2.5 and 3.5 V, respectively. Blue curve: EL spectrum at 7 V of a structure fabricated with the same specifications, except that the granularity of the ITO anode has been modified to hamper the injection of the electrons. All spectra are normalized between 0 and 1. (b) Result of the Wien radiance renormalization described in the text. (c) Black curve: same EL spectrum as the black trace in panel (a). Light-green curve: EL spectrum of a structure fabricated with the same specifications, except that the NCs have a smaller radius, shifting their bandgap by 200 nm to the blue. Dark-green curve: Wien radiance renormalization of the light-green trace.

which accounts for the spectral variations caused by the carrier temperature. To test this hypothesis, we study the response of devices subject to different excitation conditions. Figure 3(a) shows the measurements for two samples operating with the same Au rings and discs as in Fig. 2. The red, gray, and black traces are the PL spectrum and two EL spectra of the first sample taken at 2.5 and 3.5 V. The blue curve corresponds to the EL spectrum of the second structure at 7 V. Such a high bias is necessary to record this spectrum because the ITO anode has been fabricated with a smaller granularity that hampers electrical injection—and thus increases the temperature of the injected carriers.

While all devices feature the three peaks discussed previously, their spectra exhibit significant variations (note that the quasi-Fermi-level difference only affects the amplitude of the signal and not the spectrum). If, according to Eq. (1), these variations are due to differences in the carrier temperature, it should be possible to superimpose all the traces by renormalizing them with the ratio $I_W(\omega, T_i)/I_W(\omega, T_1)$, where $T_{i=1,2,3,4}$ are the carrier temperatures of the four experiments. The result of the renormalization, obtained by fitting the values of T_i and plotted on Fig. 3(b), confirms this hypothesis since all the curves become almost perfectly superimposed. It should be noted that to perform this fit, one of the temperatures must be known. Here, we have assumed that the PL experiments hardly raise the carrier temperature above that of the PbS host. We have thus set the temperature of the red PL spectrum to $T_1 = 300$ K and found that the other temperatures are $T_2 = 310$ K, $T_3 = 328$ K, and $T_4 = 387$ K for the gray, black, and blue spectra, respectively. These values are reasonable since they indicate that the carrier temperature increases with the power used to excite the devices. Importantly, the fact that all the curves of Fig. 3(a) can be superimposed does not depend on the value chosen

for T_1 (although we do not expect a significant temperature increase for the PL experiments, T_1 may actually be slightly larger than 300 K due to the excess energy of the red laser pump compared to the near infrared emission) and the fitted temperatures always evolve in the same order ($T_4 > T_3 > T_2 > T_1$).

Figure 3(b) unambiguously shows that the spectra are modulated by the Wien radiance I_W , which is the landmark signature of the thermalization of the emitter assembly. As a control experiment, we have repeated these measurements with a different source of PbS nanocrystals (see the Appendix), capped with different native ligands (oleic acid instead of TOPO), and characterized by a smaller diameter that shifts their excitonic bandgap by 200 nm to smaller wavelengths (1100 nm instead of 1300 nm). The EL spectrum of the new structure is plotted as a light-green curve on Fig. 3(c). After performing the same renormalization as above, the trace becomes similar to that of the structure already investigated in Fig. 3(a) (dark-green and black curves, respectively). In particular, the same three peaks are observed at the same wavelengths, indicating that the spectral features of the devices are largely independent of the diameter of the individual NCs. This result is consistent with the idea that after ligand exchange, the NC assembly cannot be seen as an ensemble of discrete emitters but as a collective system. As stated above, this is a necessary condition for the local Kirchhoff law and it constitutes the last element of our analysis.

IV. CONCLUSION AND PERSPECTIVES

To summarize, we show a route to simultaneously optimize the electrical and optical properties of PbS NC assemblies with a combination of ligand exchange and optical antennas. Our results can be analyzed using a local form of

the Kirchhoff law, which quantitatively accounts for both the emission enhancement and the spectral modifications of the light emission.

We conclude this study by discussing the opportunities offered by optical antennas operating with the local Kirchhoff law. First, and foremost, the relevant figure of merit for optimizing their effect is the absorption cross-section density α within the semiconducting medium. A remarkable consequence is that the antennas can be placed directly in contact with the semiconducting medium to maximize their impact. In fact, additional experiments not shown here indicate that proper electrical injection (but not optical pumping) requires a contact between the metallic antennas and the NCs and that not all metals can be used for this purpose (Al antennas, for example, do not work). This problem of electrical injection has been addressed in a separate study for NCs capped with native ligands [10].

Second, the local Kirchhoff law applies when electrons and holes thermalize and form two separate reservoirs in local thermodynamic equilibrium. Consequently, the antenna operating frequency does not need to be adjusted to a particular transition contrary to antennas acting on discrete fluorophores. In fact, one of their most enabling properties is that they can be used to recombine electrons and holes far from the band edge, and thus completely redefine the spectrum of the emitting layer. We have already given examples of radical spectral design in Figs. 2 and 3, with structures capable of extracting light over a broad range of wavelengths. As another illustration, we show in Fig. 4 how to produce narrow emission bands with antennas that maximize α for selected colors only, with the same ligand-exchanged NC films considered in Figs. 2, 3(a) and 3(b). The LED characterized in Fig. 4(a) proves that it is

possible to engineer a single-peak emission at wavelengths much smaller than both the band gap of the individual NCs [approximately 1300 nm, Fig. 1(c)] and the maximum of the assembly of ligand-exchanged NCs [approximately 1500 nm, Fig. 1(c)]. In Fig. 4(b), we present a device emitting polarized light because the absorption density is created by a plasmonic resonance along the long axis of the Au nanorods. The EL spectrum taken with the other polarization, also shown in the figure, is much weaker and very much like that obtained with the nonresonant nanodiscs in Fig. 2(c), as expected since the nanorods do not support any resonance along this polarization.

Last, it is worth noting that the optical antennas imprint a specific spatial emission profile within the active layer since the cross section α is selectively enhanced in their immediate vicinity. This opens up the possibility to create intricate luminescent patterns with spatial gradients of the light spectrum, polarization, and intensity. In this regard, the local Kirchhoff law may also be at play in the electroluminescent metamaterials operating with native TOPO ligands that we have introduced previously [9,10] because their behavior obeys the three design principles stated here (robustness to quenching even in the presence of lossy nonplasmonic nanoparticles, dramatic spectral changes, and nonuniform light emission). This hypothesis is consistent with the fact that even PbS NCs capped with long native ligands cannot be considered as a collection of individual emitters because they thermalize via Förster resonant energy transfer [17]. In fact, the phenomena reported in this work are probably not limited to PbS NCs because there exist many systems that fulfill the necessary condition of carrier thermalization (e.g., continuous thin-film semiconductors, quantum wells, organic

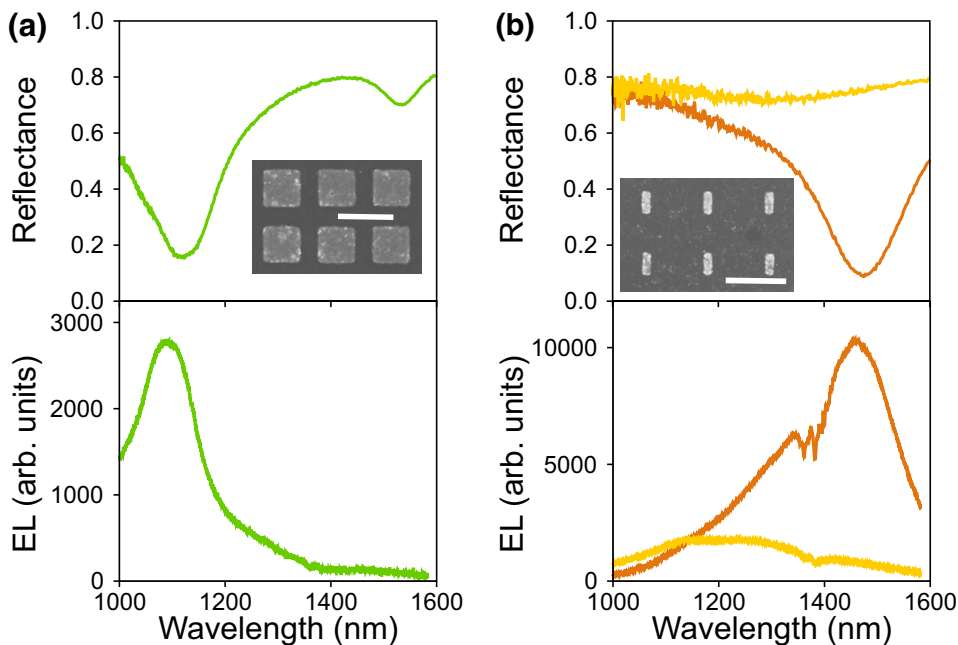


FIG. 4. (a) Reflectance and EL of a LED operating with resonant Au squares. Inset: SEM view of the Au antenna array. Scale bar: 500 nm. (b) Reflectance and EL of a LED operating with resonant Au nanorods. Orange (yellow) traces: signal measured through a polarizer aligned along the vertical (horizontal) axis of the rods. Inset: SEM view of the Au antenna array. Scale bar: 500 nm. It should be noted that all the spectra of this figure are obtained with the same assemblies of ligand-exchanged NCs as those considered in Figs. 2, 3(a) and 3(b).

dyes, ensemble of interacting emitters, etc.). It would be particularly interesting to re-examine a number of past experiments in which optical antennas were used to boost the performances of organic and quantum-dot LEDs [18–20] in view of the present results. More generally, this study provides experimental evidence that optical antennas (and, by extension, related structures such as dielectric cavities and photonic crystals) influence individual fluorophores and ensembles of emitters in radically different ways. The question of which interaction regime applies must therefore be a central question for the design of future nano-optoelectronic devices.

ACKNOWLEDGMENTS

This work was supported by the French Agence Nationale pour la Recherche (FORWARD project under Grant No. ANR-17-ERC2-0017 and GYN project under Grant No. ANR-17-CE24-0046). The sample fabrication was partly supported by the French RENATECH network.

APPENDIX: EXPERIMENTAL DETAILS

Fabrication (seven main steps): (i) Glass substrates are cleaned with ultrasound in acetone and deionized water, then treated with a Piranha solution (96% H_2SO_4 : 30% $\text{H}_2\text{O}_2 = 3:1$, v:v), H_2O -rinsed, N_2 -dried, and finally cleaned with an O_2 plasma for 5 min. (ii)–(iii) The Al electrodes and TiO_2 electron transfer layers are obtained by electron-beam evaporation of Al through a shadow mask and by spin-coating a suspension of anatase TiO_2 nanoparticles in ethanol (Ti-Nanoxide HT-L/SC, Solaronix) at 5000 rpm for 60 s onto the sample, followed by a hot plate bake at 200 °C for 15 min. (iv) The Au nanostructures are defined by electron-beam lithography using a mask of ZEP520A resist diluted in anisole (dilution ratio of 2). The writing conditions are an acceleration voltage of 80 kV, a current of 1.8 nA, and a dose of $3 \text{ C (m}^2\text{)}^{-1}$. After development of the resist, the metal nanostructures are obtained by electron-beam evaporation of 2 nm of Ti and 25 nm of Au followed by a lift-off in acetone. (v) The sample is coated with approximately 2–3 monolayers of PbS NCs and the native ligands are replaced by S^{2-} ions. In more detail, the PbS NCs are spin cast from a 15 mg ml^{-1} toluene solution at 2000 rpm for 15 s and baked on a hot plate at 150 °C for 3 min. The sample is then soaked in a solution of Na_2S in ethanol (1%) for 10 s and in ethanol for 30 s, N_2 -dried, and baked on a hot plate at 100 °C for 2 min. A second rinse in deionized water for 20 s is performed to remove any residual Na_2S . (vi)–(vii) The 10-nm-thick MoO_x layer and the ITO electrodes are deposited with a Denton sputtering system. The film of MoO_x is obtained with reactive radio frequency magnetron sputtering of a Mo target in 15% O_2 -85% Ar at a pressure of 10 μbar and a rate of 0.2 \AA s^{-1} . The ITO electrodes are made of a bilayer: one layer, which is 10-nm thick, is

deposited with a low power density ($0.65 \text{ W (cm}^2\text{)}^{-1}$) at a rate of 0.5 \AA s^{-1} to produce a polycrystalline coating with small grains designed to maximize adherence to the stack. The second layer is an 80-nm thick polycrystalline coating with larger grains, having more internal stress but a higher conductivity.

Materials and chemicals: Borosilicate glass wafer (Plan Optik AG); TiO_2 colloidal nanoparticles (Ti-Nanoxide HT-L/SC, Solaronix); sodium sulfide nonahydrate (99.99%, Sigma); Mo target (99.98%, Kurt J. Lesker); ITO target (99.99%, Kurt J. Lesker). PbS NCs: two different sources are used. Most of the results are obtained with a 2015 batch from Evident Technologies (PbS core with a 4.6-nm diameter and 2-nm-long tri-octylphosphine oxide ligands). We have also made a series of control experiments with PbS NCs from CAN Gmb (CANdots Series C, PbS core capped by oleic acid ligands). The green spectra of Fig. 3(c) are obtained with this second source of NCs.

Fourier-transform-infrared (FTIR) characterization: The FTIR measurements are performed with a Varian system equipped with an optical microscope and a Cassegrain objective focusing the incident light with a range of angles between 15 and 30°. The data are normalized by the reflectance spectrum of a Au mirror. For Fig. 4(b), an analyzer is inserted within the microscope to measure the polarization dependence of the structure.

EL and PL characterization: The light-voltage curves of Fig. 2(g) are obtained by recording at each voltage step the current and the light emitted by the device. The voltage is applied with a Keithley 2636A sourcemeter, which is also used to measure the current. The light is recorded by imaging the sample with a BX51WI Olympus microscope coupled to a Xenics Xeva 1M (In,Ga)As camera. The PL and EL spectra of Figs. 2 and 3 are also collected with this microscope (using a 50X objective for the PL spectra and a 10X objective for the EL spectra), except that the light is redirected to a Horiba Jobin-Yvon spectrometer (composed of an iHR320 monochromator and a Symphony II (In,Ga)As detector). The excitation source for the PL measurements is a He-Ne laser emitting at 632.8 nm. For the polarization dependence measurements of Fig. 3, a Glan-Thomson polarizer with a fixed angle is inserted before the spectrometer and the measurements are performed by rotating the sample with respect to this polarizer.

Absorption measurements: The measurements of Fig. 1(b) are performed with a UV-3600 spectrometer from Shimadzu.

Finite-element simulations: The simulations of Fig. 2 are performed with the RF module of the COMSOL Multiphysics package. The structures are modeled as a single unit cell flanked by periodic boundary conditions. Rather than simulating the whole stack, it is found that excellent agreement with the FTIR experiments can be obtained by merging the PbS, MoO_x , and ITO layers into a single

domain with the permittivity of ITO multiplied by a factor of 1.25 for the real part. The optical constants of the TiO₂ and ITO layers used in this model are measured with a Woollam M-2000 ellipsometer. The metal permittivities are taken from the literature. The reflectance spectra of Figs. 2(a) and 2(d) are evaluated for unpolarized light and an incident angle of 20° (to take into account that the measurements are performed with a Cassegrain objective). The fields of Figs. 2(h) and 2(i) are obtained with the same model but for linearly polarized light and under normal incidence to reveal the symmetries of the modes.

-
- [1] L. Sun, J. J. Choi, D. Stachnik, A. C. Bartnik, B.-R. Hyun, G. G. Malliaras, T. Hanrath, and F. W. Wise, Bright infrared quantum-dot light-emitting diodes through inter-dot spacing control, *Nat. Nanotechnol.* **7**, 369 (2012).
- [2] J. J. Choi, J. Luria, B.-R. Hyun, A. C. Bartnik, L. Sun, Y.-F. Lim, J. A. Marohn, F. W. Wise, and T. Hanrath, Photogenerated exciton dissociation in highly coupled lead salt nanocrystal assemblies, *Nano Lett.* **10**, 1805 (2010).
- [3] F. Xu, L. Gerlein, X. Ma, C. Haughn, M. Doty, and S. Cloutier, Impact of different surface ligands on the optical properties of PbS quantum dot solids, *Materials* **8**, 1858 (2015).
- [4] J. Gao and J. C. Johnson, Charge trapping in bright and dark states of coupled PbS quantum dot films, *ACS Nano* **6**, 3292 (2012).
- [5] C. R. Kagan and C. B. Murray, Charge transport in strongly coupled quantum dot solids, *Nat. Nanotechnol.* **10**, 1013 (2015).
- [6] J. Zhang, J. Tolentino, E. R. Smith, J. Zhang, M. C. Beard, A. J. Nozik, M. Law, and J. C. Johnson, Carrier transport in PbS and PbSe QD films measured by photoluminescence quenching, *J. Phys. Chem. C* **118**, 16228 (2014).
- [7] P. J. Roland, K. P. Bhandari, and R. J. Ellingson, Influence of interparticle electronic coupling on the temperature and size dependent optical properties of lead sulfide quantum dot thin films, *J. Appl. Phys.* **119**, 094307 (2016).
- [8] J. Gao, J. Zhang, J. van de Lagemaat, J. C. Johnson, and M. C. Beard, Charge generation in PbS quantum dot solar cells characterized by temperature-dependent steady-state photoluminescence, *ACS Nano* **8**, 12814 (2014).
- [9] Q. Le-Van, X. Le Roux, A. Aassime, and A. Degiron, Electrically driven optical metamaterials, *Nat. Commun.* **7**, 12017 (2016).
- [10] H. Wang, Q. Le-Van, A. Aassime, X. L. Roux, F. Charra, N. Chauvin, and A. Degiron, Electroluminescence of colloidal quantum dots in electrical contact with metallic nanoparticles, *Adv. Opt. Mater.* **6**, 1700658 (2018).
- [11] R. Carminati, J.-J. Greffet, C. Henkel, and J. M. Vigoureux, Radiative and non-radiative decay of a single molecule close to a metallic nanoparticle, *Opt. Commun.* **261**, 368 (2006).
- [12] L. Rogobete, F. Kaminski, M. Agio, and V. Sandoghdar, Design of plasmonic nanoantennae for enhancing spontaneous emission, *Opt. Lett.* **32**, 1623 (2007).
- [13] P. Bharadwaj and L. Novotny, Spectral dependence of single molecule fluorescence enhancement, *Opt. Express* **15**, 14266 (2007).
- [14] P. Würfel, The chemical potential of radiation, *J. Phys. C Solid State Phys.* **15**, 3967 (1982).
- [15] S. Lin, Y. Feng, X. Wen, T. Harada, T. W. Kee, S. Huang, S. Shrestha, and G. Conibeer, Observation of hot carriers existing in Ag₂S nanoparticles and its implication on solar cell application, *J. Phys. Chem. C* **120**, 10199 (2016).
- [16] J.-J. Greffet, P. Bouchon, G. Brucoli, and F. Marquier, Light Emission by Nonequilibrium Bodies: Local Kirchhoff Law, *Phys. Rev. X* **8**, 021008 (2018).
- [17] S. W. Clark, J. M. Harbold, and F. W. Wise, Resonant energy transfer in PbS quantum dots, *J. Phys. Chem. C* **111**, 7302 (2007).
- [18] A. Fujiki, T. Uemura, N. Zettsu, M. Akai-Kasaya, A. Saito, and Y. Kuwahara, Enhanced fluorescence by surface plasmon coupling of Au nanoparticles in an organic electroluminescence diode, *Appl. Phys. Lett.* **96**, 043307 (2010).
- [19] X. Ma, J. Benavides, C. R. Haughn, F. Xu, M. F. Doty, and S. G. Cloutier, High polymer-LEDs enhancement by exciton-plasmon coupling using encapsulated metallic nanoparticles, *Org. Electron.* **14**, 1916 (2013).
- [20] X. Yang, P. L. Hernandez-Martinez, C. Dang, E. Mutlugun, K. Zhang, H. V. Demir, and X. W. Sun, Electroluminescence efficiency enhancement in quantum dot light-emitting diodes by embedding a silver nanoisland layer, *Adv. Opt. Mater.* **3**, 1439 (2015).